

Improved water oxidation via Fe doping of $CuWO_4$ photoanodes: Influence of the Fe source and concentration

Yue Sun(孙岳), Fenqi Du(杜粉琦), Donghang Xie(谢东航), Dongmei Yang(杨冬梅), Yang Jiao(焦阳), Lichao Jia(贾丽超), and Haibo Fan(范海波)

Citation: Chin. Phys. B, 2020, 29 (**12**): 127801. DOI: 10.1088/1674-1056/aba9cb
Journal homepage: http://cpb.iphy.ac.cn; http://iopscience.iop.org/cpb

What follows is a list of articles you may be interested in

Thermal stability of magnetron sputtering Ge-Ga-S films

Lei Niu(牛磊), Yimin Chen(陈益敏), Xiang Shen(沈祥), Tiefeng Xu(徐铁峰)
Chin. Phys. B, 2020, 29 (**8**): 087803. DOI: 10.1088/1674-1056/aba273

Non-parabolic effect for femtosecond laser-induced ultrafast electro-absorption in solids

Li-Bo Liu(刘利博), Hong-Xiang Deng(邓洪祥), Xiao-Tao Zu(祖小涛), Xiao-Dong Yuan(袁晓东), Wan-Guo Zheng(郑万国)
Chin. Phys. B, 2020, 29 (**1**): 017801. DOI: 10.1088/1674-1056/ab577c

Influence of annealing treatment on the luminescent properties of Ta:β-Ga_2O_3 single crystal

Xiaowei Yu(余小威), Huiayuan Cui(崔慧源), Maodong Zhu(朱茂东), Zhilin Xia(夏志林), Qinglin Sai(赛青林)
Chin. Phys. B, 2019, 28 (**7**): 077801. DOI: 10.1088/1674-1056/28/7/077801

Temperature and excitation dependence of stimulated emission and spontaneous emission in InGaN epilayer

Xuee An(安雪娥), Zhengjun Shang(商正君), Chuanhe Ma(马传贺), Xinhe Zheng(郑新和), Cuiling Zhang(张翠玲), Lin Sun(孙琳), Fangyu Yue(越方禹), Bo Li(李波), Ye Chen(陈晔)
Chin. Phys. B, 2019, 28 (**5**): 057802. DOI: 10.1088/1674-1056/28/5/057802

Photodetectors based on inorganic halide perovskites: Materials and devices

Ying Li(李营), Zhi-Feng Shi(史志锋), Xin-Jian Li(李新建), Chong-Xin Shan(单崇新)
Chin. Phys. B, 2019, 28 (**1**): 017803. DOI: 10.1088/1674-1056/28/1/017803

Improved water oxidation via Fe doping of $CuWO_4$ photoanodes: Influence of the Fe source and concentration*

Yue Sun(孙岳)[1], Fenqi Du(杜粉琦)[1], Donghang Xie(谢东航)[1], Dongmei Yang(杨冬梅)[1], Yang Jiao(焦阳)[1], Lichao Jia(贾丽超)[2,†], and Haibo Fan(范海波)[1,‡]

[1] *School of Physics, Northwest University, Xi'an* 710069, *China*

[2] *School of Material Science and Engineering, Shaanxi Normal University, Xi'an* 710119, *China*

(Received 27 May 2020; revised manuscript received 16 July 2020; accepted manuscript online 28 July 2020)

Iron (Fe) was successfully doped in $CuWO_4$ photoanode films with a combined liquid-phase spin-coating method via the dopant sources of $Fe(NO_3)_3$, $FeSO_4$ and $FeCl_3$. The microstructure of the prepared films was characterized by x-ray diffraction, scanning electron microscopy, and atomic force microscopy. The light absorption and photoelectric conversion properties were evaluated by the UV-visible absorption spectra and monochromatic incident photon-to-electron conversion efficiency. The chemical composition and element combination of the samples were examined by x-ray photoelectron spectroscopy. A linear sweep voltammetric and stability test (*I*–*t*) were performed with an electrochemical workstation. The results show that the samples are uniform with a thickness of approximately 800 nm and that the photoelectrochemical performance of the doped films is heavily dependent on the Fe source and dopant concentration. Upon optimizing the doping conditions of $Fe(NO_3)_3$ and the optimal source, the photocurrent density in the Fe-doped $CuWO_4$ photoanode film is improved by 78% from 0.267 mA/cm^2 to 0.476 mA/cm^2 at 1.23 V vs reversible hydrogen electrode. The underlying causes are discussed.

Keywords: photoanode thin film, liquid phase method, $CuWO_4$, Fe doping

PACS: 78.40.Fy, 78.56.–a **DOI:** 10.1088/1674-1056/aba9cb

1. Introduction

In the face of increasingly severe problems of climate and environment,[1] the development of new ways to obtain clean energy and the discovery of new energy sources have long been matters of discussion. Photoelectrochemical (PEC) oxidation in water is a new approach to obtaining clean energy.[2] As a promising material facilitating clean energy, semiconductors offer substantial application prospects.[3] At present, the semiconductors known to catalyze PEC oxidation include TiO_2,[4] ZnO,[5] and $CuWO_4$.[6] Among them, $CuWO_4$, with its advantages of a narrow band gap,[7] ideal stability and partial visible light absorption, has been a focus in science research for decades. Thang *et al.* have studied the magnetic ordering, electronic structure and oxygen vacancy of $CuWO_4$ theoretically. They described the electronic structure of $CuWO_4$ by adopting first principles without using any adjusted parameters.[8] However, $CuWO_4$ has disadvantages such as low photoelectric current density, low incident photo-to-electron conversion efficiency (IPCE) and poor charge separation efficiency.[9] To overcome such limitations, the strategy typically adopted is to form heterostructures coupled with other materials, and some advances have been made in this area. For instance, Chen *et al.* investigated cobalt phosphate (CoPi) deposited on $CuWO_4$ thin films by an electrodeposition method and recorded an 86% higher photocurrent response than that of unmodified $CuWO_4$.[10] By the sol-gel synthesis method, Zhang *et al.* loaded $CuWO_4$ thin films with Ag nanowires, which can increase the carrier mobility. A fourfold improvement in photocurrent to 1.5 mA/cm^2 was identified at 1.23 V vs the reversible hydrogen electrode (RHE) with a Faradaic efficiency of the catalyst of approximately 31%.[11] It has also been found that the photocurrent can be enhanced greatly by the formation of a $BiVO_4/CuWO_4$ heterojunction, which favors charge carrier separation and collection.[12,13] By constructing nanosword-like $VO_2/CuWO_4$ heterojunctions, a reasonably high photodegradation efficiency was obtained over the short term, making this device promisingly applicable for highly efficient photocatalytic process.[14] Liu *et al.* designed a highly efficient $Pt/CuWO_4/Co_3O_4$ photoanode system for PEC water splitting. This novel ternary $Pt/CuWO_4/Co_3O_4$ structure was found to exhibit a prominently enhanced photocurrent of 4.4 mA/cm^2 at 1.23 V vs the RHE.[15] When synthesizing $CuWO_4$ nanoflake (NF) array films, hydrogen treatment[16] and hole scavenger addition[17] can also effectively improve the PEC activity.

Doping cations is another popular method to address the limitations of $CuWO_4$. Compared with heterojunctions, this

*Project supported by the National Natural Science Foundation of China (Grant No. 11204238) and the Natural Science Foundation of Shaanxi Province, China (Grant No. 2017JM1030).

†Corresponding author. E-mail: lichaojia@snnu.edu.cn

‡Corresponding author. E-mail: hbfan@nwu.edu.cn

© 2020 Chinese Physical Society and IOP Publishing Ltd

approach has the advantage of simple preparation. For example, Bohra *et al.* studied the PEC performance of Fe-doped films and found that doping $FeSO_4$ alone can not significantly improve the PEC performance of the film. Under the dual effects of doping and hole scavenging, the PEC performance was greatly improved.[18] Li *et al.* improved the PEC performance of $CuWO_4$ by doping F, and a doping content of 2.50 at.% in $CuWO_4$ showed the highest photocurrent density of 0.57 mA·cm^{-2} at 1.23 V vs the RHE.[19] Yang *et al.* reported that Mo-doping $CuWO_4$ not only narrowed the bandgap but also significantly improved the electron density, with both benefiting the PEC performance in the oxygen evolution reaction.[20] Tri *et al.* investigated the effect of V doping on the photocatalytic performance of $CuWO_4$ and found that it improved the charge transfer properties as well as preventing electron and hole recombination.[21] Among these dopants, Fe is a very promising choice because of its low cost and nontoxicity. Nevertheless, to our knowledge, the effect of the Fe source and the dopant concentration on Fe-doped $CuWO_4$ PEC performance has not yet been systematically studied.

Therefore, in this article, the catalysis ability in PEC oxidation of Fe-doped $CuWO_4$ with different valance states and dopant concentrations is investigated comprehensively. Pristine and Fe-doped $CuWO_4$ films from various Fe dopants are successfully synthesized by employing a combined liquid-phase spin-coating method. The structure, optical features, and morphology are examined. The effects of various Fe dopants with respect to the dopant concentration on the PEC behavior are investigated and compared, and the optimum doping reagent and concentration are identified.

2. Experimental section

2.1. Materials

$Cu(NO_3)_2{\cdot}3H_2O$, $(NH_4)_6H_2W_{12}O_{40}{\cdot}4H_2O$, $C_6H_8O_7{\cdot}H_2O$, ethylene glycol (EG), $Fe(NO_3)_3{\cdot}9H_2O$ and $FeSO_4{\cdot}7H_2O$ were purchased from Merck. $FeCl_3{\cdot}6H_2O$ was purchased from Aladdin. All reagents were analytically pure and did not require further purification.

2.2. Experimental procedure

In the experiment, $Cu(NO_3)_2{\cdot}3H_2O$ and $(NH_4)_6H_2W_{12}O_{40}{\cdot}4H_2O$ were used as raw materials. Citric acid, carbamide, F-127, and F-108 were used as admixtures. Deionized water (hereafter written as H_2O) and EG were used as the solvent of $(NH_4)_6H_2W_{12}O_{40}{\cdot}\,4H_2O$ and $Cu(NO_3)_2{\cdot}\,3H_2O$, respectively. The EG stabilized the solution and reduced solid agglomeration to a certain extent. All chemicals and reagents were of the highest purity available. The detailed experimental procedures were as follows.

The fluorine-doped tin oxide (FTO), which was selected as the substrate, was ultrasonically cleaned for 30 min in H_2O, acetone, and EG sequentially and dried in a drying oven just before use.

Weighed raw materials and admixtures were transferred to glassware, and then the solvents (H_2O, EG) were injected by pipettes. The two solutions were stirred for 1 hour by a magnetic stirrer; then, the $Cu(NO_3)_2{\cdot}3H_2O$ solution was transferred to the $(NH_4)6H_2W_{12}O_{40}{\cdot}4H_2O$ solution, and the mixture was stirred for additional 1 hour.

After adjusting the speed of rotation and duration of the spin coater, the FTO glass was placed on the rotating plate, affixed by vacuum. A 0.3 mL sample of the evenly stirred solution was dropped onto the center of the FTO glass by a pipette, and then the spin coater was activated. The samples were then transferred to a drying oven and dried at 80 °C for 10 min. Both coating and drying were repeated for a total of eight times.

The samples were then placed in a muffle furnace, and the heating rate was adjusted to 3 °C/min. The furnace temperature was maintained for 2 h after reaching 500 °C and then allowed to cool naturally. In early experiments, it was found that better crystallization performance could be demonstrated by double annealing.

2.3. Method of representation

An XRD-6000 diffractometer was used to characterize the phase and structure of prepared samples by recording the x-ray diffraction (XRD) pattern. Cu $K\alpha$ radiation (40 kV and 30 mA) was used, and the scanning angles ranged from 10.0° to 70.0°. The step size and scanning rate were 0.02° per step and 0.2 s per step, respectively. The peaks in the $CuWO_4$ pattern were compared with the corresponding standard (JCPDS 73-1823). The grain size of the sample was calculated using the Scherrer formula

$$D = \frac{K\gamma}{B\cos\theta}, \tag{1}$$

where K and γ are constants (0.89 and 0.154056 nm, respectively), B is the full width at half maximum (FWHM), and θ is the diffraction angle.[22]

The surface appearance of the sample was observed using an FE-SEM SU-8020 (Hitachi) tool under an acceleration voltage of 3.00 kV and high vacuum.

A TU-1901 double-beam UV-visible (UV-vis) spectrophotometer was used to record the absorption property of the samples at a fixed wavelength ranging from 750 nm to 350 nm. The bandgap of the samples was calculated by the formula[23]

$$\left(\frac{Ahv}{K}\right)^{1/2} = hv - E_g, \tag{2}$$

where A is the absorbance and K is a constant related to the material and test conditions, which does not affect the value of the band gap. Here, hv can be replaced by $1024/\lambda$.

X-ray photoelectron spectroscopy (XPS) is an important surface analysis technique used mainly to determine the chemical composition of samples and the chemical state of elements. In our experiment, a ThermoFisher ESCALAB 250Xi tool was used to record the XPS spectra of the samples.

An atomic force microscope (AFM, AFM-Icon, Bruker) was used to determine the nano-scale surface topography of the sample by tapping mode.

To perform linear sweep voltammetric (LSV), a CH Instruments 760E electrochemical workstation was used for photoelectric chemical performance testing. All PEC measurements were conducted in a customized unit with a quartz observation window. The $CuWO_4$ thin film was used as the photoanode, Ag/AgCl (saturated KCl) was used as the reference electrode, and a Pt auxiliary electrode was used to complete the three-electrode voltammetry setup. The experiments were all carried out in a sodium sulfate (Na_2SO_4) electrolyte solution at 0.1 mol/L with pH = 6.8. The LSV rate under light was 10 mV/s. The light source simulates a solar radiation intensity of 100 mW/cm^2 and shines through the front of a quartz window (area: 0.25 cm^2) onto the $CuWO_4$ film. The photocurrent can be recorded by the optical power meter to construct the required chart.

The stability of the photoanode material was tested by the CH Instruments 760E electrochemical workstation as well. The photocurrent of the sample was measured over a certain duration under a certain voltage (0.63 V) and light exposure (30 s with light and 30 s without light) for stability characterization.

To determine the IPCE under the conditions of fixed bias and different wavelengths, the photocurrent density of the sample was tested and recorded, and then the IPCE of the sample was calculated by the formula

$$\mathrm{IPCE} = \frac{I}{P} \times \frac{1240}{\lambda} \times 100\%. \tag{3}$$

where I is the photocurrent density, and P is the calibrated optical power density at the incident wavelength λ.[24]

2.4. $CuWO_4$ film doping

The liquid-phase method[25] is a simple and widely used doping method. The advantages of this method in controlling the composition proportion and doping make it of great research value. Therefore, in the experiment, we first aimed to grow $CuWO_4$ thin films on the FTO substrate by the liquid-phase method combined with the spin-coating method. The doping level can be adjusted by changing the concentration of ions in the precursor solution. In the doping process, the doped ions replace the donor atoms, resulting in changes of parameters such as the oxidation state, particle size, electron configuration, and abundance and toxicity. We selected Fe ions as the doped ions.[26,27] By considering the system and diversity of dopant selection, three inorganic salts of iron were chosen as the dopants, namely, $Fe(NO_3)_3$, $FeSO_4$ and $FeCl_3$. Although there are two valence states of Fe ions, i.e., Fe^{3+} and Fe^{2+}, in the dopants, Fe^{2+} is thermodynamically and kinetically easy to oxidize to Fe^{3+}. Thus in this case, the ultimate doping should be all Fe^{3+}, which is nonisovalent doping and will increase the concentration of the carriers in the thin film, thus improving the electronic conductivity.[18] The goal was ultimately to identify the samples providing the best performance.

3. Results

3.1. Pristine $CuWO_4$ films

The structural and optical properties of the prepared pristine $CuWO_4$ samples were first examined. As shown in Fig. 1(a), the typical surface morphology, obtained by scanning electron microscopy (SEM), exhibits compact homogeneous nanoparticles. The cross-sectional images reveal that the thickness of the film is approximately 800 nm, as shown in Fig. 1(b). From reference to the AFM images (Figs. 1(c) and 1(d)), the size of the $CuWO_4$ nanoparticles is approximately 40 nm, and the microscopic structure of the samples is uniform.

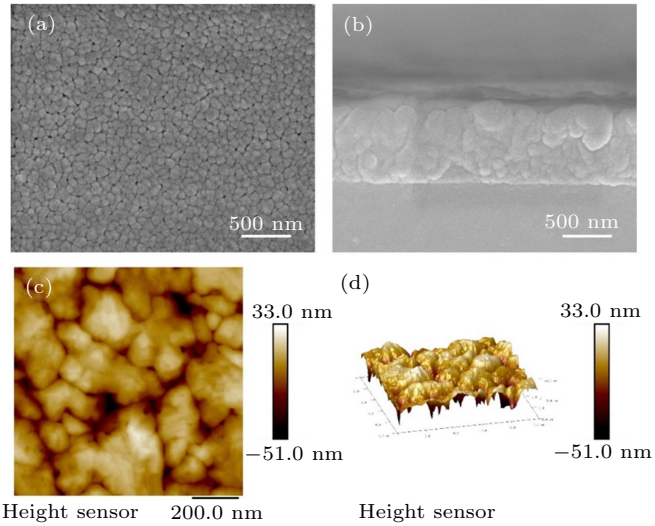


Fig. 1. (a) Top-view and (b) cross-sectional view SEM images of the pristine $CuWO_4$ film, (c) 2D and (d) 3D AFM images of the pristine $CuWO_4$ film.

$CuWO_4$ is an n-type semiconductor and an indirect band gap material.[28,29] Figure 2(a) shows the UV-visible absorption spectrum of the prepared pristine $CuWO_4$ thin film. The sample absorbs visible light to a certain extent. The bandgap of the sample calculated by the formula (1) is approximately 2.2 eV. The results are consistent with the previous reports of $CuWO_4$ thin films[9,29,30] and single crystals.[7,31] Figure 2(b) shows the photocurrent density-potential response of the pristine $CuWO_4$ film. The abscissa represents the electric potential of the reference electrode, while the ordinate represents the photocurrent density. The photocurrent onset potential is approximately 0.75 V vs the RHE. Above this value, the photocurrent increases linearly as the potential increases, illustrating the good stability of the prepared photoanode in different

potential regions. All potentials in this work are reported with reference to Ag/AgCl and an RHE. The potential vs Ag/AgCl was converted into the potential vs the RHE on the basis of the following equation:[24]

$$E_{\mathrm{RHE}} = E_{\mathrm{Ag/AgCl}} + 0.0591\mathrm{pH} + 0.1976, \quad (4)$$

where pH scale measures how acidic or basic the substance is. When the electric potential of the reference electrode reaches 0.63 V, the potential of water reaching oxidation–reduction equilibrium is 1.23 V, corresponding to an ordinate value of 0.267 mA/cm^2 as labeled in the figure.

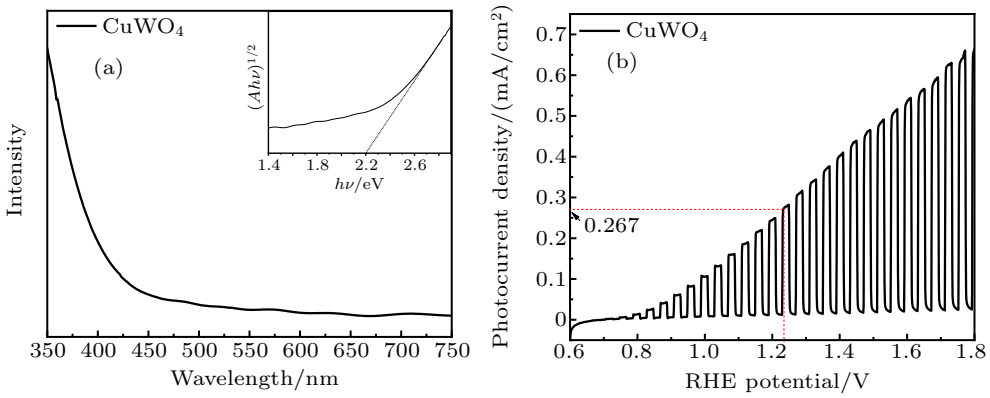


Fig. 2. (a) UV-vis absorption spectra of the pristine $CuWO_4$ films. (b) Photocurrent density-potential response of the pristine $CuWO_4$ film. The red dashed line signifies 1.23 V vs. RHE potential and the photocurrent density is 0.267 mA/cm^2 obtained at this potential.

3.2. $CuWO_4$ films doped with different iron salts

Figure 3 shows the AFM images of the samples doped with different iron salts. The surfaces of the samples feature accumulated nanoparticles with little variation as a result of the low dopant content. Figure 4 shows the roughness values of the samples as detected by AFM and expressed with the root-mean-square roughness (R_q) and arithmetic mean roughness (R_a). The roughness of the film increases slightly after doping, which is due to the stress from Fe doping. Replacement of the Cu atoms by Fe atoms produces lattice distortion, resulting in an increase in roughness.

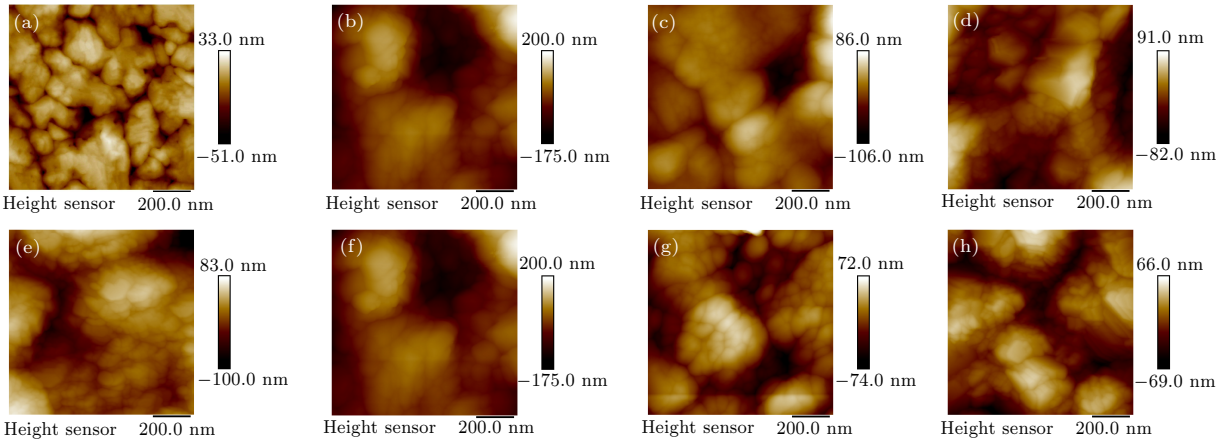


Fig. 3. AFM images of samples doped with different dopants (a) in the pristine $CuWO_4$ film, (b) 0.3% $Fe(NO_3)_3$, (c) 0.3% $FeSO_4$, (d) 0.3% $FeCl_3$; and AFM images of samples doped with $Fe(NO_3)_3$ in the concentrations of (e) 0.15%, (f) 0.3%, (g) 0.6%, (h) 0.9%.

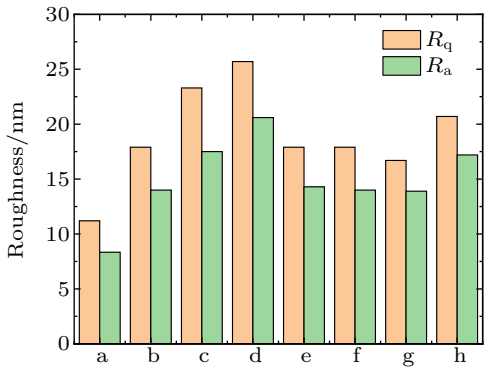


Fig. 4. Roughness of samples doped with different iron salts, the denotation of the letters on the abscissa is same as that in Fig. 3.

To further verify successful doping, XPS measurements were carried out to provide not only the elemental composition but also the chemical states. Figure 5(a) shows the whole XPS spectra of the pristine and doped films. The peaks of both the pristine $CuWO_4$ and the samples doped with Fe^{3+} look very similar, and the intensity of the XPS peaks of the sample doped with Fe^{2+} is rather weak. Figure 5(b1) shows the XPS Cu 2p spectrum of the pristine $CuWO_4$ film, and the peaks at 934.3 eV and 954.3 eV correspond to the Cu $2p_{2/3}$ and Cu $2p_{1/3}$ orbits of Cu^{2+}, respectively.[32] Figure 5(b2) suggests that the peak of Cu 2p narrows upon doping with $Fe(NO_3)_3$.

The reason is likely that Cu ions are replaced by Fe ions. The W 4f spectral region of the pristine $CuWO_4$ film is shown in Fig. 5(c1); the $W4f_{7/2}$, W $4f_{5/2}$ and W $5p_{3/2}$ peaks are respectively gathered at 35.3 eV, 37.4 eV and 41.1 eV, which are consistent with the standard binding energies of W^{6+} at oxidation states.[33] Figure 5(c2) shows that the W 4f feature peaks shift slightly toward higher binding energies when the sample is doped with $Fe(NO_3)_3$. This phenomenon can be explained by the doping reducing the lattice constant and the loss of electrons in the outer layer of the atomic orbital. For instance, the excursion of the electron cloud toward other elements weakens the shielding effect and increases the binding energy. In Fig. 5(d1), the O 1s peak is deconvoluted into two peaks, corresponding to the oxygen states of W–O (530.2 eV) and surface OH^- (531.8 eV).[34,35] In Fig. 5(d2), the peaks are shifted slightly toward higher binding energies. This may be due to the increased concentration of O after doping.[36] Because the radius of the doped ions is different from that of the matrix ions they replace, the introduction of impurities inevitably causes local crystal lattice distortion, resulting in the conversion of part of the crystal lattice oxygen to adsorbed oxygen and the migration of binding energy.

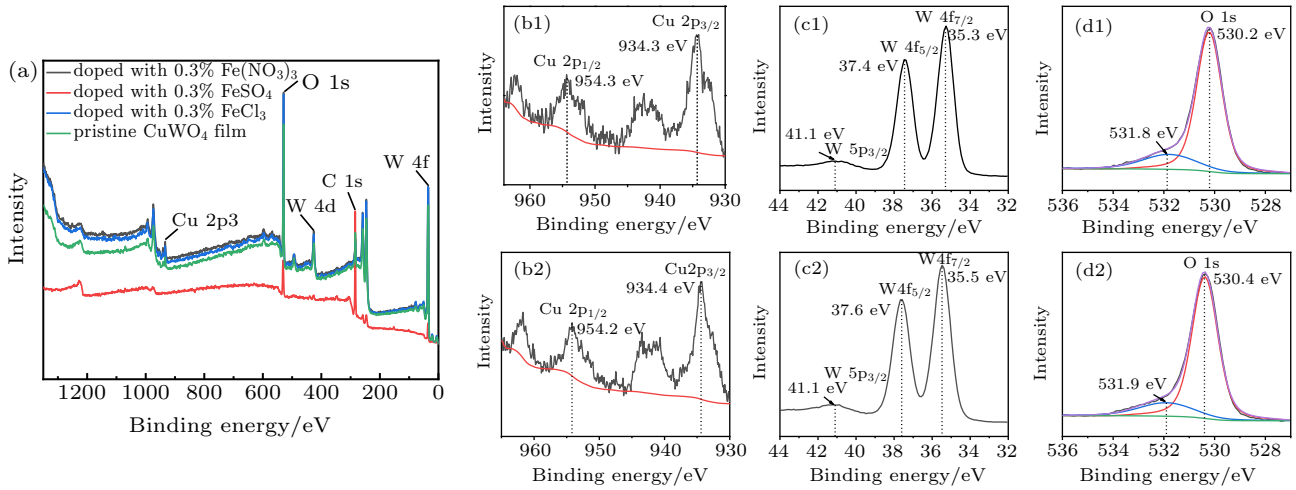


Fig. 5. (a) XPS spectra of prepared samples, (b1) Cu 2p peak, (c1) W 4f peak, (d1) O 1s peak; and XPS spectra of samples doped with $Fe(NO_3)_3$ (b2), Cu 2p peak (c2), W 4f peak, (d2) O 1s peak.

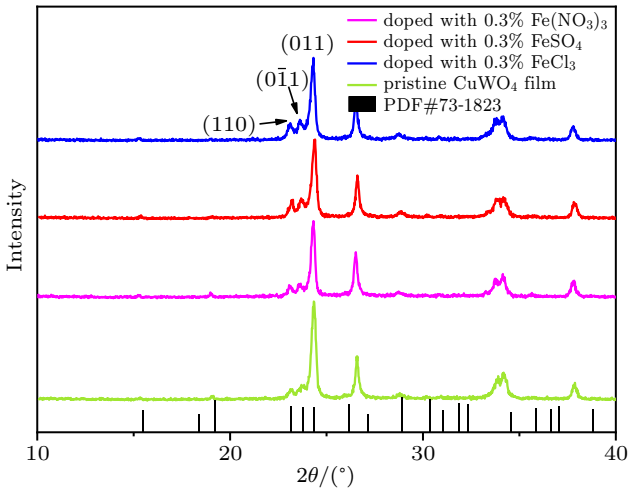


Fig. 6. XRD patterns of $CuWO_4$ films doped with $Fe(NO_3)_3$, $FeSO_4$, $FeCl_3$.

The crystal structures of the pristine samples and samples doped with different iron salts were characterized by x-ray diffraction (XRD), and the results are presented in Fig. 6. Diffraction peaks appear at 18.94°, 23.13°, 23.53°, 24.34°, corresponding to the (100), (110), (0$\bar{1}$1) and (011) faces of $CuWO_4$, respectively. The intensity of the (011) peak is greatest, which means that the $CuWO_4$ films were grown with (011) orientation. The Fe phase cannot be observed from the figures, which is attributed to the low Fe dopant content. From the Scherrer formula (1) and as listed in Table 1, the grain size of the pristine $CuWO_4$ film is approximately 39.97 nm, and the grain size of the samples increases slightly upon doping, which matches well with the AFM results. In addition, a slight shift of the (011) peaks to smaller angles can be observed, which means that stress is exerted on the $CuWO_4$ lattice. Again, this phenomenon is always observed in doped semiconductors.

Table 1. Grain size (D/nm) of the $CuWO_4$ films doped with different dopants.

Dopant	Pristine	$Fe(NO_3)_3$	$FeSO_4$	$FeCl_3$
$2\theta/(°)$	24.34	24.32	24.36	24.32
FWHM/(°)	0.28	0.26	0.24	0.24
D/nm	39.97	43.95	45.72	47.61

UV-vis absorption spectra were collected to evaluate the capacity for light absorption of the samples doped with different iron salts, and the results are shown in Fig. 7. Compared with the other samples, the absorption strength of the sample doped with $Fe(NO_3)_3$ is most improved. The light absorption performance of the sample doped with $FeSO_4$ is essentially unchanged, or even slightly decreased. In comparison with the absorption edges of the pristine and $FeSO_4$-doped samples, those of the two Fe^{3+}-doped samples are shifted to-

ward the visible region. The observed red shift is ascribed to the narrowing of the band gap caused by an increase in grain size, which can be further verified by the Tauc plots of $CuWO_4$ films doped with different iron salts. As shown in Fig. 8 the band gap energy of the samples doped with 0.3% $Fe(NO_3)_3$, 0.3% $FeCl_3$, 0.3% $FeSO_4$ and the pristine $CuWO_4$ are 1.91 eV, 2.12 eV, 2.22 eV, and 2.2 eV, respectively. These results confirm that Fe doping narrows the bandgap of $CuWO_4$.

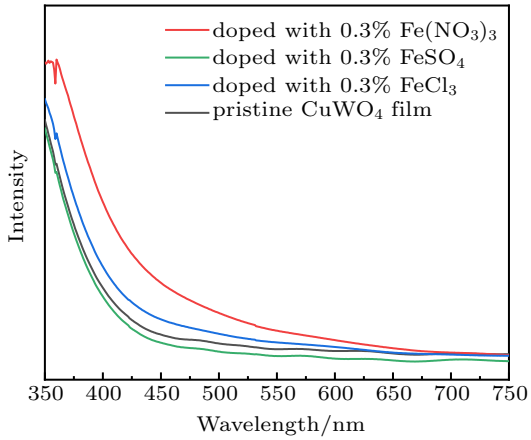


Fig. 7. UV-vis spectra of $CuWO_4$ films doped with $Fe(NO_3)_3$, $FeSO_4$, $FeCl_3$.

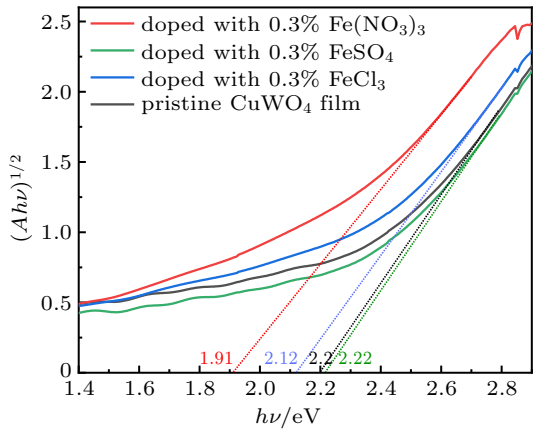


Fig. 8. Tauc plots of $CuWO_4$ films doped with $Fe(NO_3)_3$, $FeSO_4$, $FeCl_3$.

IPCE measurements were also performed on the samples and are compared in Fig. 9. At the same conditions and concentration, the film doped with 0.3% $Fe(NO_3)_3$ has the highest IPCE. A comparison with the results in Figs. 7 and 8 clearly shows that the high absorption and narrow band gap dominate the increase in IPCE.

Figure 10 shows the photocurrent density-potential response of the samples doped with different iron salts under chopped light illumination. A clear increase in the photocurrent density of all the samples can be seen upon doping with 0.3% iron salts. The photocurrent density at the water splitting potential reaches its maximum of 0.476 mA/cm^2 when the sample is doped with $Fe(NO_3)_3$. Furthermore, the photocurrent enhancement increases sharply at higher bias voltages. This is because photon-generated carriers at a higher bias potential can reach the photoanode-electrolyte interface more easily. Hence, the doped samples with a greater carrier density in the bulk present a much larger photocurrent. The appearance of dark current in the samples can also be observed in Fig. 10. Such a phenomenon also suggests that doping leads to crystal defects in the surface of the film. The film performs best when doped with 0.3% $Fe(NO_3)_3$.

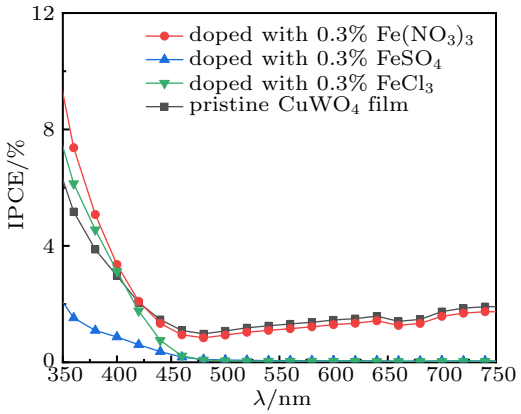


Fig. 9. IPCE curves of $CuWO_4$ films doped with $Fe(NO_3)_3$, $FeSO_4$, $FeCl_3$.

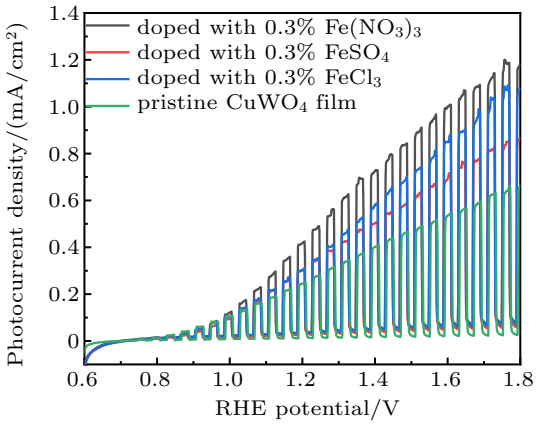


Fig. 10. Photocurrent density-potential response of the $CuWO_4$ films doped with $Fe(NO_3)_3$, $FeSO_4$, $FeCl_3$.

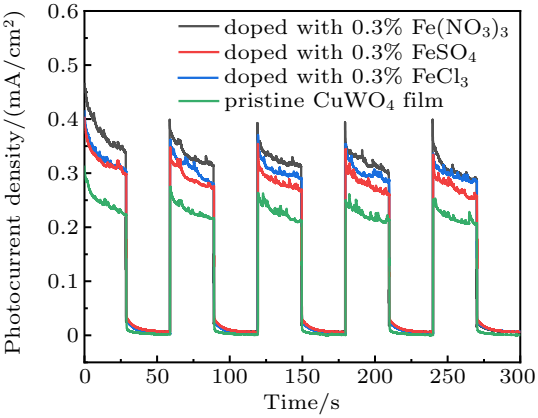


Fig. 11. The *I*–*t* curves of $CuWO_4$ films doped with $Fe(NO_3)_3$, $FeSO_4$, $FeCl_3$.

Figure 11 shows the *I*–*t* curves of prepared samples doped with different iron salts. The curves are obtained at a bias voltage of 0.63 V with 30 s of light supply and 30 s without light.

The photocurrent density of these doped samples attenuates within 100 s and then tends to be stable. It is concluded that doping does not affect the stability of the samples.

3.3. $CuWO_4$ films doped with $Fe(NO_3)_3$ in different concentrations

In the comparison and analysis of the samples doped with different iron salts, the conclusions of all representations matched and indicate that the films performed best when doped with $Fe(NO_3)_3$. Therefore in this part, the performance of the films doped with $Fe(NO_3)_3$ at different concentrations is analyzed to identify the optimum doping concentration.

XRD figures of samples doped with $Fe(NO_3)_3$ at different concentrations are shown in Fig. 12. The figure reinforces that the films are grown with (011) preference, as mentioned above. As listed in Table 2, with increasing $Fe(NO_3)_3$ concentration, the intensity of the (011) diffraction peaks decreases slightly, and the FWHM progressively narrows. This combined effect causes the size of the grains to gradually increase with increasing doping concentration, and no Fe-related phase is observed. This phenomenon verifies that the Fe atoms were successfully doped in the lattice and substituted at the Cu sites, in turn causing defects and increasing the disorder of the samples.

Table 2. Grain size (D/nm) of the $CuWO_4$ films doped with $Fe(NO_3)_3$ in different concentrations.

Doping concentration	Pristine	0.15%	0.3%	0.6%	0.9%
$2\theta/(^\circ)$	24.34	24.38	24.32	24.32	24.31
FWHM/(°)	0.28	0.25	0.26	0.23	0.21
D/nm	39.97	43.06	43.95	45.71	54.99

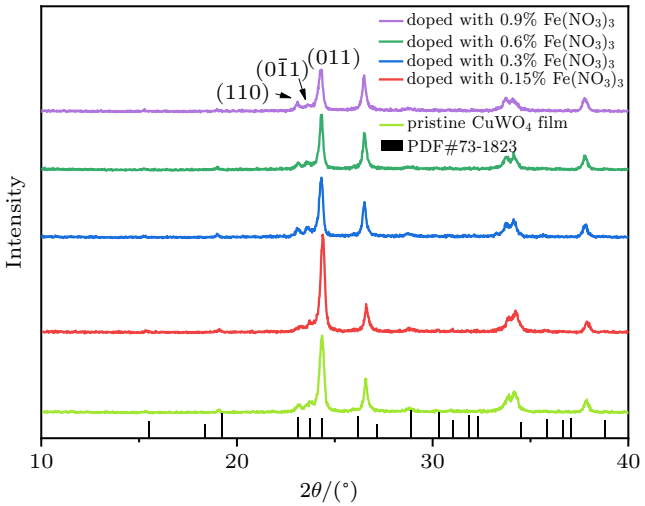


Fig. 12. XRD patterns of $CuWO_4$ films doped with $Fe(NO_3)_3$ in different concentrations.

The UV-vis spectra of $CuWO_4$ films doped with $Fe(NO_3)_3$ at different concentrations, as shown in Fig. 13, indicate that the absorbed band ranges mainly from 300 nm to 450 nm and that the doping concentration has a remarkable effect on absorption. The sample exhibits the maximum absorption intensity when doped with 0.3% $Fe(NO_3)_3$. Figure 14 shows Tauc plots of $Fe(NO_3)_3$-doped $CuWO_4$ films, from which the bandgap energy can be deduced as 2.2 eV, 2.18 eV, 1.91 eV, 1.94 eV and 1.84 eV for the pristine films and 0.15%, 0.3%, 0.6% and 0.9% $Fe(NO_3)_3$ concentrations, respectively. These results confirm that $Fe(NO_3)_3$ doping can regulate the bandgap of $CuWO_4$ to a certain extent by varying the $Fe(NO_3)_3$ doping concentration.

Figure 15 presents the varying IPCEs of the samples with

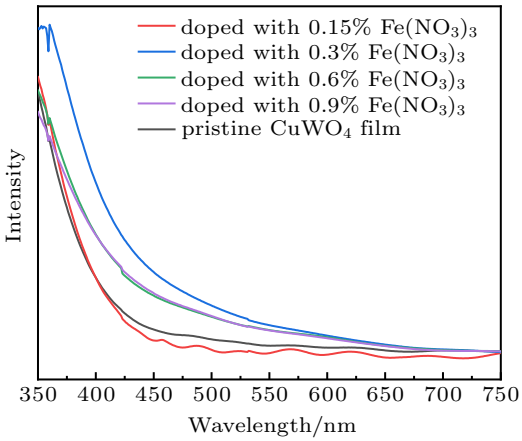


Fig. 13. (a) UV-vis spectra of $CuWO_4$ films doped with $Fe(NO_3)_3$ in different concentrations.

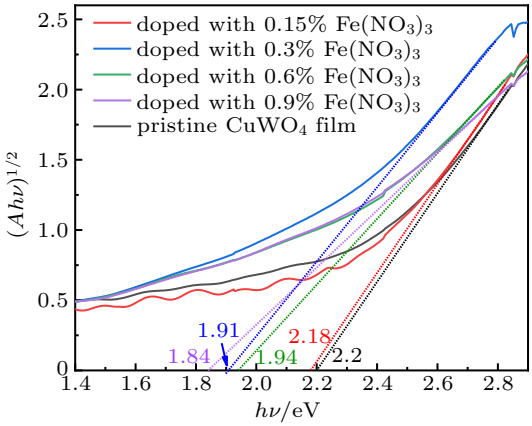


Fig. 14. Tauc plots of $CuWO_4$ films doped with $Fe(NO_3)_3$ in different concentrations.

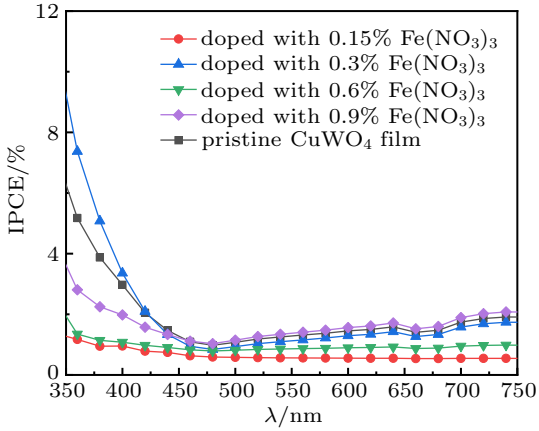


Fig. 15. IPCE curves of $CuWO_4$ films doped with $Fe(NO_3)_3$ in different concentrations.

different doping concentrations. It can be concluded that the moderate doping level, i.e., 0.3%, is the best choice and that doping at too high or too low a concentration is unfavorable for photo-to-electron conversion. Specifically, when the doping concentration is too high, the dopant tends to agglomeration, undergoing surface enrichment to form a new phase, which reduces the effective area of the photocatalytic material and decreases the photoelectric conversion efficiency. This conclusion is consistent with the measured absorption properties.

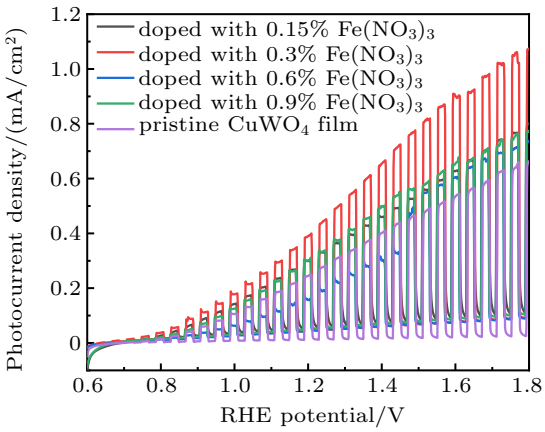


Fig. 16. Photocurrent density-potential response of $CuWO_4$ films doped with $Fe(NO_3)_3$ in different concentrations.

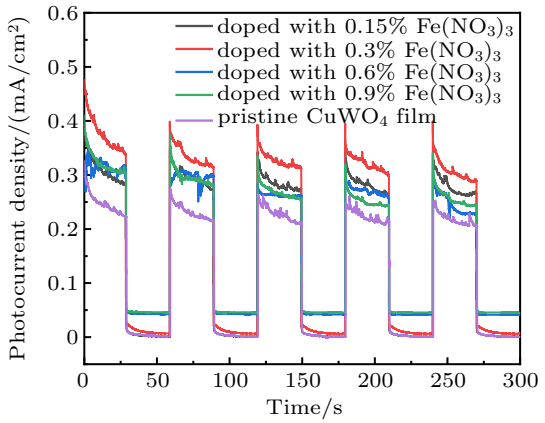


Fig. 17. The *I*–*t* curves of $CuWO_4$ films doped with $Fe(NO_3)_3$ in different concentrations.

PEC measurements of the prepared samples were conducted and are compared in Fig. 16. The photocurrent density exhibits clear variation for samples with different doping concentrations. The sample doped with 0.3% $Fe(NO_3)_3$ presents the best results, with an optimized value of 0.476 mA/cm^2 at the water splitting potential, which can be ascribed to its strong light absorption and high IPCE. The curves of photocurrent density versus time, as shown in Fig. 17, can be used to assess the dynamics of water oxidation. The test bias was set at 0.63 V, and the interval time (with and without light supply) was 30 s. After the first cycle, the photocurrent density for all the samples tended to be stable, and the value for the optimal sample was maintained above 0.3 mA/cm^2. This result demonstrates the remarkable stability of the samples prepared by this method toward PEC oxidation application in water. In addition, very high doping levels leads to degeneration in the crystal quality, which causes the dark current in the sample to become prominent.

3.4. Discussion

From the results presented above, we can conclude that the Fe sources and concentrations of the doping Fe ions have significant effects on the crystal quality, light absorption, and IPCE and thus the PEC performance of the Fe-doped $CuWO_4$ films, and the possible reasons are discussed here. Firstly, doping produces local lattice defects in a semiconductor that capture photogenerated electrons and holes, inhibit their recombination, and enhance the photocatalytic activity of the material. Secondly, doping Fe can affect the energy level structure of $CuWO_4$, causing the original energy level to be hybridized, so that the photons with small energy can also be captured, thereby improving the light absorption performance and ultimately improving the photocatalytic activity. Thirdly, the species of the Fe source have great influence on the aborption property of the Fe-doped films. Because the Fe^{2+} will convert to Fe^{3+} finally and could not make any difference in the final reactant, the reason for this big difference should be related with the anions. During the annealing process at 500 °C, the NO_3^- and Cl^- are easily wiped out by forming vapor product through the thermal decomposition of the reaction by-product of NH_4NO_3 and NH_4Cl due to their low decomposition temperature,[37,38] which favors the purity of the $CuWO_4$ and consequently the absorption property. Nevertheless, the leaving of sulfate ions in $(NH_4)_2SO_4$ usually occurs between 550 and 650 °C,[39] so the SO_4^{2-} is difficult to be transformed into a gaseous state and will stay in the system during the annealing process, which will prevent the efficient doping of Fe ions and deteriorate the property of the film. Speaking of the comparison of the $Fe(NO_3)_3$ and $FeCl_3$, because Cl^- has a strong coordination ability with Fe^{3+} and may form the complex $FeCl_4^-$,[40,41] $Fe(NO_3)_3$ can provide a higher doping efficiency than $FeCl_3$. Fourthly, as for the Fe^{3+} doping concentration, when the Fe concentration is too low, although the crystal quality is good, doping has almost no effect on the bandgap or light absorption. By increasing the Fe doping concentration to a moderate level, the bandgap energy of the doped $CuWO_4$ can be reduced significantly, and the light absorption is enhanced, which definitely improves the PEC performance. When the concentration of Fe is higher than a certain value, the spacing between the trapping sites of photogenerated electrons and holes decreases, and the probability of recombination by capturing photogenerated electrons and holes increases. As a result, the photocatalytic activity is significantly reduced. At this level, however, the dopants tend to agglomerate, resulting in surface enrichment or even the formation of new phases.[42]

4. Summary

Uniform Fe-doped $CuWO_4$ thin films with a thickness of approximately 800 nm have been prepared via a two-step approach using a liquid phase and spin coating. By comparing the crystal quality, absorption, IPCE and PEC performance, it can be concluded that $Fe(NO_3)_3$ is the best choice as an Fe dopant because of its high doping efficiency. The optimal doping concentration of $Fe(NO_3)_3$ is shown to be 0.3% due to the coordination of the strongest light absorption and the highest IPCE. After optimizing the doping conditions, the photocurrent density of the film is improved by 78% from 0.267 mA/cm^2 to 0.476 mA/cm^2, and a possible mechanism is proposed. This work demonstrates that $Fe(NO_3)_3$ is a promising dopant for $CuWO_4$ films, with potential applications in solar water splitting.

Acknowledgement

The authors thank AiMi Academic Services (www.aimieditor.com) for English language editing and review services.

References

[1] Maeda K and Domen K 2010 *J. Phys. Chem. Lett.* **1** 2655
[2] Nozik A J 1978 *Ann. Rev. Phys. Chem.* **29** 189
[3] Zhang P, Zhang J and Gong J 2014 *Chem. Soc. Rev.* **43** 4395
[4] He Y, Sutton N B, Rijnaarts H H M and Langenhoff A A M 2016 *Appl. Catalysis B* **189** 283
[5] Zheng L, Zheng Y, Chen C, Zhan Y, Lin X, Zheng Q and Wei K 2012 *Chempluschem* **77** 217
[6] Lhermitte C R and Bartlett B M 2016 *Acc. Chem. Res.* **49** 1121
[7] Lacomba-Perales R, Ruiz-Fuertes J, Errandonea D, Martinez-Garcia D and Segura A 2008 *Europhys. Lett.* **83** 37002
[8] Ho Viet T, Albanese E and Pacchioni G 2019 *J. Phys.: Condens. Matter* **31** 145503
[9] Yourey J E, Kurtz J B and Bartlett B M 2012 *J. Phys. Chem. C* **116** 3200
[10] Chen S, Hossain M N and Chen A 2018 *ChemElectroChem* **5** 523
[11] Zhang H, Yilmaz P, Ansari J O, Khan F F, Binions R, Krause S and Dunn S 2015 *J. Mater. Chem. A* **3** 9638
[12] Pilli S K, Deutsch T G, Furtak T E, Brown L D, Turner J A and Herring A M 2013 *Phys. Chem. Chem. Phys.* **15** 3273
[13] Ye W, Chen F, Zhao F, Han N and Li Y 2016 *ACS Appl. Mater. Interfaces* **8** 9211
[14] Dashtian K, Ghaedi M, Shirinzadeh H, Hajati S and Shahbazi S 2018 *Chem. Eng. J.* **339** 189
[15] Liu Z, Song Q, Zhou M, Guo Z, Kang J and Yan H 2019 *Chem. Engin. J.* **374** 554
[16] Hu D, Diao P, Xu D, Xia M, Gu Y, Wu Q, Li C and Yang S 2016 *Nanoscale* **8** 5892
[17] Gao Y and Hamann T W 2017 *J. Phys. Chem. Lett.* **8** 2700
[18] Bohra D and Smith W A 2015 *Phys. Chem. Chem. Phys.* **17** 9857
[19] Li C and Diao P 2020 *Electrochim. Acta* **352** 136471
[20] Yang J, Li C and Diao P 2019 *Electrochimica Acta* **308** 195
[21] Tri N L M, Trung D Q, Thuan D V, Dieu Cam N T D, Al Tahtamouni T, Pham T D, Duc D S, Thanh M H T, Ha H V, Thu N H A and Trang H T 2019 *Int. J. Hydrogen Energy* **45** 18186
[22] Scherrer P 1918 *Göttinger Nachrichten Math. Phys.* **1918** 98
[23] Girtan M and Folcher G 2003 *Surf. Coat. Technol.* **172** 242
[24] Abdi F F and Krol F V D 2012 *J. Phys. Chem. C* **116** 9398
[25] Jakhmola P, Jha P K and Bhatnagar S P 2016 *Appl. Nanosci.* **6** 673
[26] Khyzhun O Y, Bekenev V L and Solonin Y M 2009 *J. Alloys Compounds* **480** 184
[27] Lalic M V, Popovic Z S and Vukajlovic F R 2012 *Comput. Mater. Sci.* **63** 163
[28] Ruiz-Fuertes J, Errandonea D, Segura A, Manjon F J, Zhu Z and Tu C Y 2008 *High Press. Res.* **28** 565
[29] Yourey J E and Bartlett B M 2011 *J. Mater. Chem.* **21** 7651
[30] Gaillard N, Chang Y, DeAngelis A, Higgins S and Braun A 2013 *Int. J. Hydrogen Energy* **38** 3166
[31] Doumerc J P, Hejtmanek J, Chaminade J P, Pouchard M and Krussanova M 1984 *Phys. Status Solidi A* **82** 285
[32] Novakov T 1971 *Phys. Rev. B* **3** 2693
[33] Penner S, Liu X, Kloetzer B, Klauser F, Jenewein B and Bertel E 2008 *Thin Solid Films* **516** 2829
[34] Khyzhun O Y, Strunskus T, Cramm S and Solonin Y M 2005 *J. Alloys and Compounds* **389** 14
[35] Chen H and Xu Y 2015 *RSC Adv.* **5** 8108
[36] Zhang Y, Du G, Wang X, Li W, Yang X, Ma Y, Zhao B, Yang H, Liu D and Yang S 2003 *J. Cryst. Growth* **252** 180
[37] Izato Y I, Kajiyama K and Miyake A 2014 *Sci. Technol. Energ. Mater.* **75** 128
[38] Olszak-Humienik M 2001 *Thermochim. Acta* **378** 107
[39] Bokhimi X, Morales A, Ortiz E, Lopez T, Gomez R and Navarrete J 2004 *J. Sol-Gel Sci. Technol.* **29** 31
[40] Rabex J F, linden L A, Kaczmarek H, Qu B J and Shi W F 1992 *Ploymer Degradation and Stability* **37** 33
[41] Liu J, Zhang W, Liang C and Sun Z 2010 *J. University of Jinan* **24** 135
[42] Zhou G, Liu S and Peng D 1996 *Chin. J. Chem. Phys.* **9** 54